Physics of Fluids

Finite obstacle effect on the aerodynamic performance of a hovering wing

Cite as: Phys. Fluids **31**, 101902 (2019); https://doi.org/10.1063/1.5119046
Submitted: 09 July 2019 . Accepted: 13 September 2019 . Published Online: 04 October 2019

B. Yin, G. Yang, and P. Prapamonthon

Physics of Fluids ARTICLE scitation.org/journal/phf

Finite obstacle effect on the aerodynamic performance of a hovering wing

Cite as: Phys. Fluids 31, 101902 (2019); doi: 10.1063/1.5119046
Submitted: 9 July 2019 • Accepted: 13 September 2019 •
Published Online: 4 October 2019

B. Yin,[1,a] G. Yang,[1] and P. Prapamonthon[1,2]

AFFILIATIONS

[1] Key Laboratory for Mechanics in Fluid Solid Coupling Systems, Institute of Mechanics, Chinese Academy of Sciences, Beijing, China

[2] Department of Aeronautical Engineering, International Academy of Aviation Industry, King Mongkut's Institute of Technology Ladkrabang, Bangkok, Thailand

[a] **Electronic mail:** yinbo@imech.ac.cn

ABSTRACT

The finite obstacle effect on the aerodynamic performance of a normal hovering wing is studied using the immersed boundary method. Phenomena of a two-dimensional wing hovering above, under, or on the side of a circular obstacle are presented. Parameters including obstacle size, distance, location, and flapping angle are investigated to study how the aerodynamic force and flow field are affected. The diameter of the obstacle ranges from 0.5*c* to 12*c* and the distance between the centroid of the wing and obstacle surface from 0.5*c* to 6*c* (*c* is the wing chord length). Previous observations of ground effects including force enhancement, reduction, and recovery occur similarly when the wing hovers above the obstacle of diameter greater than 2*c*. However, finite obstacles affect the aerodynamic performance differently when the size shrinks to a critical value. Force drops when the wing moves close and rises when moving away, opposite to the ground effect. As flapping angle amplitude increases, the force change tends to be consistent for different-sized obstacles. The top or side effect shows a different influence on the force change. Force monotonically increases as the distance decreases when the wing hovers under the obstacle. The side effect places a less important factor on the aerodynamic performance. All force changes under such circumstance are less than 13% referring to nonobstacle result. The gap between the leading or trailing edge of the wing and obstacle surface plays a significant role in the leading and trailing edge vortices generating, shedding, and pairing, which greatly affects the force change.

I. INTRODUCTION

Insect flight has been attracting scientists for decades because it inspired the invention of the novel micro-aerial vehicle (MAV), which has vast potential applications including environmental protection and rescuing.[1,2] Different from fixed wings, insects generate lift and thrust by a highly unsteady flapping motion.[3–6] Extensive studies have been conducted previously to discuss the mechanisms of insect flapping flight as well as fish swimming.[7] The main mechanisms include delayed stall, fast pitching rotation, and wake-capture effect. As the quasisteady theory[8] is not suitable to explain the unsteady, large angle of attack (AoA), and high-lift flapping flight, Ellington *et al.*[9] concluded that the stall delay due to the leading edge vortex (LEV) remarkably enhances the lift. The LEV leads to a strong and prolonged suction effect on the condition of a low Reynolds number (Re), which is proved to play the most significant role in the high lift generation. Besides the LEV, fast pitching rotation, and wake capture also contribute to the force increase and peak value during cyclic motion.[10,11] Furthermore, researchers also investigated the interaction among multiple wings and explored the wing-wing effects and the optimum distance.[12,13] Much numerical and experimental work has been done to study the combined effect of the LEV, pitching rotation, and wake capture and discuss the aforementioned mechanisms.[14–20]

Considering the real nature other than ideal lab configuration, insects often fly in the presence of boundaries, finite of infinite. One typical scenario is that insects land on or take off from the ground. Gao and Lu[21] studied insect normal hovering above the infinite ground by two-dimensional numerical simulation. They pointed out that during normal hovering, three regimes of ground effect are identified: force enhancement, reduction, and recovery, depending on the distance to the ground, which obviously differs from

the force change of a fixed wing in the proximity of the ground.[22] Such force change is closely associated with vortical structures and the interaction between the leading/trailing edge vortex (TEV) and the wing. Furthermore, Lu *et al.*[23] conducted the digital particle image velocimetry (DPIV) experiment to study the two-dimensional ground effect, which matches the computational results. To consider a more realistic situation, three dimensional numerical and experimental studies have also been carried out.[24–28] Lu *et al.*[26] conducted both 3D simulation and experiment on the ground effect. It shows that the 3D results are similar to that of 2D; however, the ground effect is relatively weak. However, other researchers like Su[27] and Kolomenskiy[28] claimed that the ground effect on flapping wings is negligible.

Aforementioned studies all consider the full ground effect on the insect landing or taking off. However, in the real world, there are more circumstances with finite boundaries than infinite ground/wall, such as approaching or perching on fruit, flower, and rock. Wang[29] investigated the partial ground effect, which helps to understand the aerodynamics when the MAV lands on the edge of a platform. This study reveals lift-modifying mechanisms not observed before under infinite ground effect. However, the research on the finite boundary effect is still lacking. Meng[30] discussed the ceiling effects on the aerodynamics of a hovering wing and pointed out that the reason for the force enhancement is the increase in the relative velocity and the angle of attack of the wing. For the future design and control of novel MAVs, it is of great importance to understand the aerodynamics when the MAV flies closely to finite boundaries under various circumstances. So in this paper, the finite boundary effect is numerically simulated and discussed to reveal what is the similarity and difference with the ground effect.

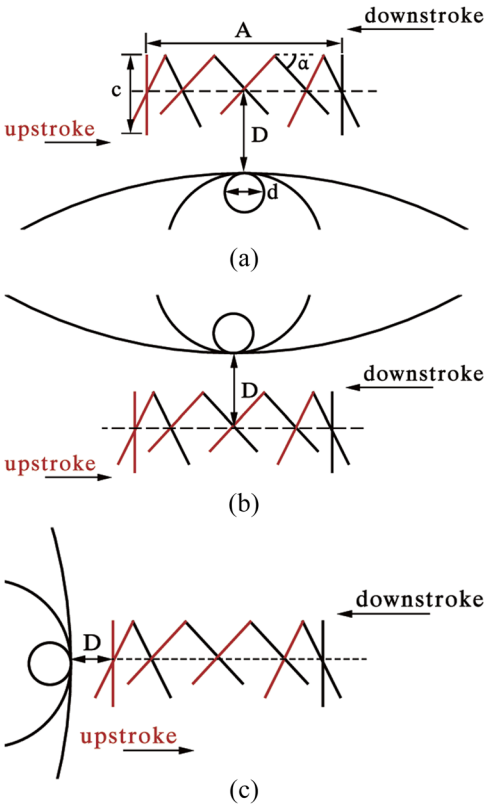

FIG. 1. Schematic of a two-dimensional wing hovering in proximity of different-sized circular obstacles: (a) above, (b) under, and (c) on the right side.

II. PROBLEM DESCRIPTION

A two-dimensional rigid plate with chord length c and negligible thickness is considered as the research model shown in Fig. 1. In fact, according to the insect flight, a complete hovering cycle consists of two translational directions: downstroke and upstroke and two rotational motions: supination and pronation. To simplify the real flight, a combined translational and rotational motion is specified mathematically at the leading edge as follows:[31]

$$x(t) = \frac{A}{2}\cos(2\pi ft), \tag{1}$$

$$\alpha(t) = \alpha_0 + \beta\sin(2\pi ft + \phi), \tag{2}$$

where $x(t)$ represents the horizontal position of the leading edge (LE), $\alpha(t)$ means the angle from the horizontal axis to the leading edge (in the counterclockwise direction)—flapping angle, $y(t)$ of LE is unchanged, A is the stroke distance of the LE—flapping amplitude, α_0 is the initial orientation, β is the flapping angle amplitude, f is the flapping frequency, and ϕ is the phase difference between rotation and translation. In the current work, we focus on the normal hovering, so α_0 is chosen as $-\pi/2$. According to the previous study,[21] ground effect shows similarity among different phases, so we select $\phi = 0$, representing the symmetrical rotation.

To study the finite obstacle effect, a two-dimensional cylinder of diameter d serves as the obstacle in the simulation. The center of the cylinder is set at the origin. The wing hovers in the proximity of the obstacle subject to Eqs. (1) and (2). When hovering above or under the obstacle, the distance between cylinder top or bottom point and stroke midline is marked as D in Figs. 1(a) and 1(b). The stroke midline is parallel to the LE motion trajectory, passes through midchord point at the initial stage, and perpendicular to D. When hovering on the side in Fig. 1(c), D means the distance between the side point of the cylinder and the midchord point of the wing at the closest position. To parameterize the system, we define the nondimensional groups including the normalized stroke distance, Reynolds number, normalized obstacle diameter, and gap distance, which are given by

$$\frac{A}{c}, \quad Re = \frac{\pi Afc}{\nu_f}, \quad r = \frac{d}{c}, \quad \frac{D}{c}. \tag{3}$$

III. NUMERICAL METHOD

The flow is governed by the viscous incompressible Navier–Stokes equation and the continuity equation, nondimensionalized as follows:

$$\frac{\partial \tilde{v}_i}{\partial \tilde{t}} + \frac{\partial \tilde{v}_j \tilde{v}_i}{\partial \tilde{x}_j} = -\frac{\partial \tilde{p}}{\partial \tilde{x}_i} + \frac{1}{Re}\frac{\partial^2 \tilde{v}_i}{\partial \tilde{x}_j^2}, \tag{4}$$

$$\frac{\partial \tilde{v}_i}{\partial \tilde{x}_i} = 0, \tag{5}$$

where all items in the above equations are dimensionless: $\tilde{v}_i$ is the fluid velocity, $\tilde{p}$ is the field pressure, and Re is the Reynolds number defined in Eq. (3). No-slip and no-penetration conditions are imposed at the flow–solid boundary. The initial flow field is quiescent, and the computational domain is large enough to keep the far field undisturbed.

The governing equations (4) and (5) are numerically solved in an implicit manner by an in-house solver. A sharp-interface immersed-boundary method developed on the basis of previous studies[32,33] is employed to deal with the rigid stationary and moving boundaries. The concept of sharp-interface IBM is to define ghost nodes near the fluid–solid interface, which generate assisting body intercept and image point to satisfy the velocity and pressure boundary conditions. The Navier–Stokes equation is discretized on a single-block Cartesian grid and solved using standard central finite difference scheme. A three-step projection method is employed: for each time step, the advection-diffusion equation is first solved to obtain the intermediate velocity field, and then RHS of the Poisson equation is assembled and solved according to the intermediate velocity to get the pressure field, finally the velocity field is corrected and time moves on. In the computation, the zero thickness wing is treated with an artificial thickness of about three times of the grid spacing and adapts to the local grid refinement. The solid wing is represented by a set of Lagrangian points, evenly distributed along the chord length. The circumference of the cylinder also has the same representation and distribution of Lagrangian points as the solid wing does.

IV. SIMULATION SETUP AND VALIDATION

In this paper, the Reynolds number is chosen as 200 and the stroke distance $A/c = 2.5$. These parameters are chosen from the published literature[4,29,34] on insect flight. To investigate the aerodynamic performance under various circumstances, the obstacle size, position, and the flapping angle amplitude are discussed in the paper. The normalized obstacle size r is selected as 0.5, 1, 2, 4, 8, and 12 to cover a wide range of finite obstacle and study the difference and similarity among these sizes and ground effect. The wing hovers above, under, and on the side of the obstacle, representing the possible situation in the real environment. The flapping angle amplitude β (=$\pi/8$, $\pi/4$ and $\pi/3$) is also investigated, considering the insect could adjust the flapping angle to remain stable flight.

The whole computational domain is $20c \times 35c$ of Cartesian grids and large enough to eliminate the potential numerical perturbation from domain boundaries. Uniform (both in x- and y-directions) and dense mesh spread in the core area of $3c \times 10c$ with spacing $\Delta x = \Delta y = 0.02c$. The surrounding region is nonuniformly meshed to reduce the grid number and limit computational cost. The entire domain consists of a Cartesian grid of 320 × 528. The time step is set as $\Delta t = 0.002T$, where $T = 1/f$ is the period of one flapping cycle.

The lift and drag coefficients are calculated and compared to evaluate the aerodynamic performance, defined as in Eq. (6),

$$C_L = \frac{F_L}{(0.5\rho_f U^2 c)}, \qquad C_D = \frac{F_D}{(0.5\rho_f U^2 c)}, \tag{6}$$

where F_L and F_D denote the forces in vertical and horizontal directions by integrating the shear stress and pressure acting on the wing body. F_L is always positive upward and negative downward. F_D is positive against the flapping direction and negative following the direction. ρ_f stands for the air density, the reference velocity U (=πAf) is the maximum flapping velocity of leading edge, and c is the wing chord length. Other than the forces, power consumption and efficiency are important factors. The power consumption is defined as

$$P = \mathbf{F} \cdot \dot{x} + \mathbf{M} \cdot \dot{\alpha}, \tag{7}$$

where $\mathbf{F}$ and $\mathbf{M}$ are the driven force and torque acting on the leading edge to keep the wing kinematics, respectively. Following the conservative assumption that negative input power in either translation or rotation is no longer usable, we define the positive power consumption P_+, which is the summation of the positive value of each term in Eq. (7). The positive power coefficient and lift-to-power ratio are defined, respectively, as follows:

$$C_{P_+} = \frac{P_+}{(0.5\rho_f U^3 c)}, \qquad \frac{C_L}{C_{P_+}}. \tag{8}$$

Based on the setups, the solver is validated by comparing results with Refs. 31 and 34 in Fig. 2, where curves agree well with each other. Note that all the results are rescaled using the definition in Eq. (6), different from using the maximum quasisteady lift coefficient in Ref. 31. Readers are referred to papers[35–39] for more validations of the in-house solver and its applications in flapping wings.

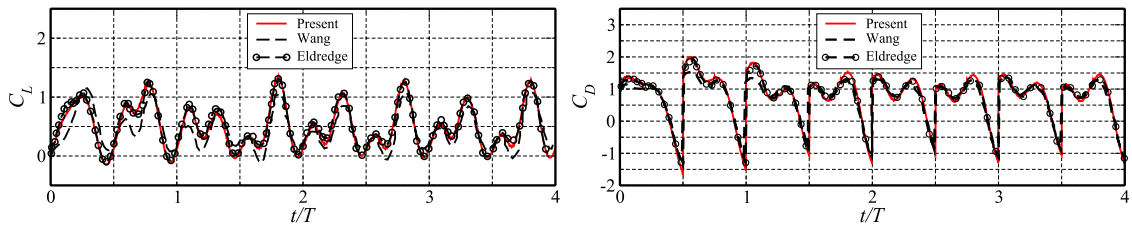

FIG. 2. (a) Lift and (b) drag coefficients (C_L and C_D) from present simulation, Wang[34] (dash line) and Eldredge[31] (dash-circle line).

V. RESULTS AND DISCUSSION

A. Effect of down obstacle

Simulation results are given and discussed by analyzing the aerodynamic forces as well as the power consumption and efficiency when the wing hovers in the proximity of the obstacle. First, the effect of obstacle size is investigated when the wing hovers vertically above the obstacle. Such circumstance represents the ground effect when the insect takes off or lands on a finite solid surface, which lacks discussion in previous studies. The nondimensional obstacle size r ranges from 0.5 to 12, and it can be predicted that when the size exceeds a certain value, the obstacle effect will approach the infinite ground effect. Figure 3 summarizes the time-averaged coefficients over 15 flapping cycles with respect to surface clearance (D/c). A dashed line representing the coefficients with no obstacle (C_L = 0.78 and C_D = 1.31) is drawn in each figure as a comparison, denoted by **NO**, namely, nonobstacle. The most significant observation in Figs. 3(a) and 3(b) is that the lift and drag change for small obstacles differ from large ones. All the lift and drag curves show a V-shape trend for $r \geq 2$, which has three stages: force enhancement, reduction, and recovery, similarly as observed in previous studies on ground effect. For lift, larger $r(\geq 2)$ results in a more enhanced value at $D/c = 1$. As D/c enlarges, the forces decrease and reach the minimum value at a certain clearance: $D/c = 2$ for $r = 2$ and $D/c = 3$ for $r \geq 4$. The minimum lift coefficients are generally similar around 0.55. For drag, the V-shape curves for $r = 2$ and 4 shift down to some extent such that the drag coefficients are below the **NO** value at $D/c = 1$. Then, the curves decrease and reach the minimum C_D around 0.9 at $D/c = 2$. For C_D of $r = 8$ and 12, the values remain above the **NO** value at $D/c = 1$ and decrease to the minimum value 0.9 at $D/c = 3$. Finally, when the wing moves further away from the obstacle, all the acting forces increase and recover to the value of free hovering for $r \geq 2$. However, as the r shrinks to 0.5 and 1, the force changes show a reversed trend: reduction, enhancement, and recovery, which is contrary to the large obstacle or infinite ground effect. Both lift and drag are reduced at $D/c = 1$, compared with $C_{L,\mathbf{NO}}$ and $C_{D,\mathbf{NO}}$, so that flapping close to small obstacles may cause potential danger because of lift force decrease. Then, forces increase as D/c grows, exceed $C_{L,\mathbf{NO}}$ and $C_{D,\mathbf{NO}}$ when $D/c > 3$, reach the maximum value at $D/c = 4$, then fall back, and gradually approach the nonobstacle value as the clearance continues enlarging to infinity. At $D/c = 4$, C_L and

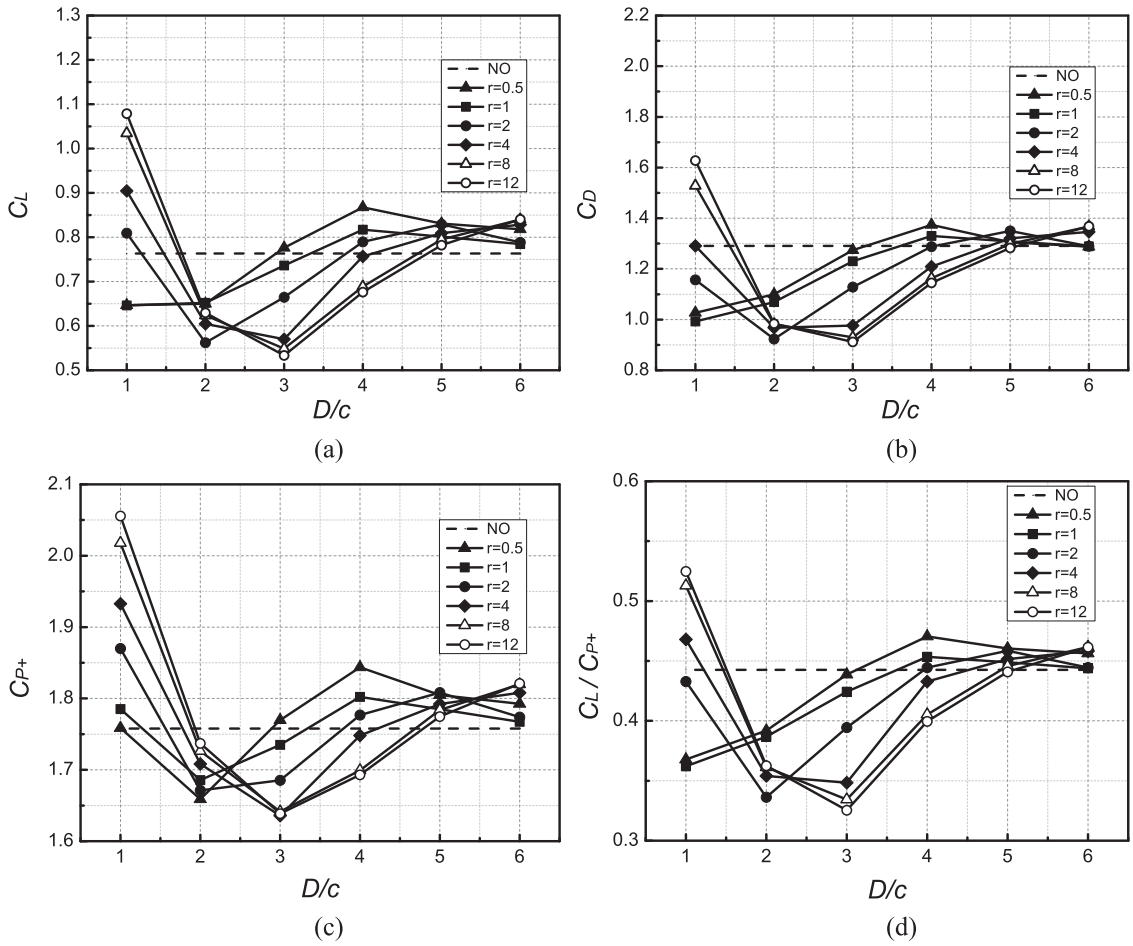

FIG. 3. Time-averaged coefficients when the wing hovers above the obstacle: (a) lift coefficient, (b) drag coefficient, (c) power coefficient, and (d) lift-to-power ratio.

C_D increase as the obstacle size diminishes. So C_L and C_D for $r = 0.5$(0.87 and 1.37) are higher than that of $r = 12$(0.68 and 1.15).

The curves in Figs. 3(c) and 3(d) show the power and efficiency change with respect to the distance: larger obstacle ($r \geq 2$) leads to more power consumption as well as higher efficiency (evaluated by C_{P+} and C_L/C_{P+}) at $D/c = 1$ because of enhanced lift generation. As the clearance increases, the curves of large obstacles decrease to a minimum value at $D/c = 3$, which is similar to the force V-shape change. On the contrary, flapping near small obstacle ($r \leq 1$) generates less force but consumes more power at $D/c = 1$, which causes low efficiency as shown in Fig. 3(d). Then, C_{P+} decreases to the minimum at $D/c = 2$, reaches a high peak at $D/c = 4$, and approaches the **NO** dash line gradually. The C_L/C_{P+} curves of $r = 0.5$ and 1 are quite similar to curves of C_L and C_D. Generally, it may cause potential risk close to smaller obstacles due to both the lift and power efficiency decrease.

To analyze the mechanism accountable for such observation, we examine the force histories and flow fields of three regions: close ($D/c < 3$), medium ($3 \leq D/c < 5$), and recovery distances ($D/c \geq 5$).

1. Close distance region

Figure 4 displays the time-dependent lift, drag, and power coefficients over one cycle in close distance of $D/c = 1$ for $r = 0.5$, 4, and 12 with the **NO** coefficient as reference. The lift and drag coefficient curves are quite periodic between upstroke and downstroke because of the symmetric flapping motion. Generally, two high peaks show up in the lift and drag curves during the downstroke. The first lift peak of curve of $r = 0.5$ occurs at $t/T = 0.05$(0.55) due to the generation of the strong vortex from the start of wing stroke. Compared with $r = 0.5$, larger r leads to higher lift and curve of $r = 12$ shows the highest lift value at $t/T = 0.05$(0.55). The first peak of $r = 0.5$ is lower than that of **NO**. As time goes toward $t/T = 0.15$(0.65), the curve of $r = 0.5$ decreases to the low peak like nonobstacle situation, while the other two curves still keep increasing owing to the obstacle effect. After $t/T = 0.15$(0.65), the three curves reach the second high lift peak around $t/T = 0.3$(0.8) because of the rotational circulation and increased flapping angle during the translation. Just before finishing the upstroke at $t/T = 0.48$(0.98), the lift curves reach the low peak as the wing pitches down and is about to reverse the stroke. The high and low peaks of each C_D history are generally in phase with C_L. During one half stroke, the first high C_D peak of $r = 12$ is somehow delayed ($t/T = 0.1$) and clearly above that of $r = 0.5$ and 4 ($t/T = 0.05$). The second high C_D peaks of three curves are quite close or even overlapped ($t/T = 0.3$). The high and low peaks of power input show up just after or before the stroke reversal ($t/T = 0.15$ and 0.45) because of the maximum inertial acceleration of deceleration. The peak value of C_P rises as the obstacle size increases, and all greater than the **NO** curve.

Figure 5 displays the vorticity contour associated with the force histories. The vortex shedding direction becomes much more horizontal no matter what the obstacle size is, which keeps the vortices

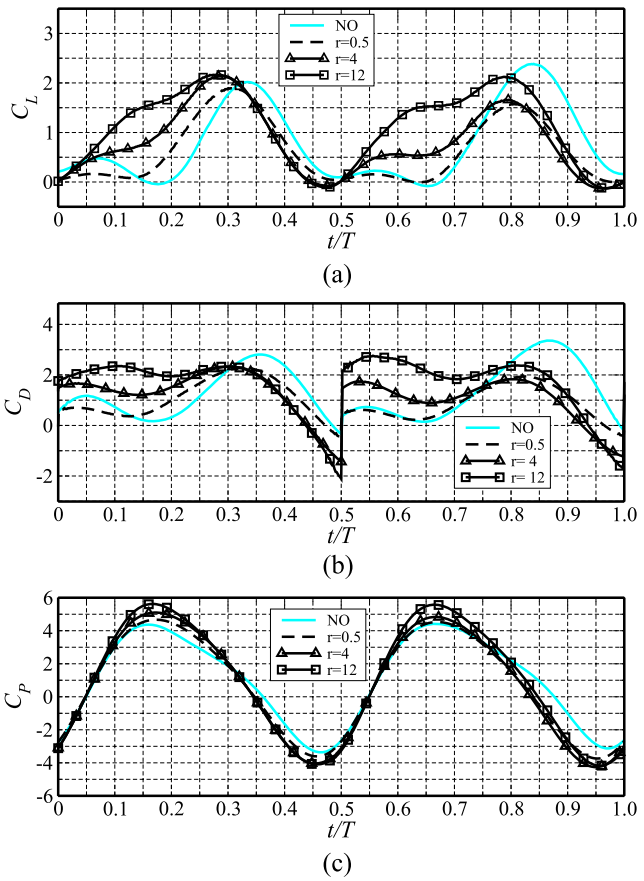

FIG. 4. Histories of (a) lift, (b) drag, and (c) power coefficients for $r = 0.5$, 4, 12, and nonobstacle in one cycle when the wing hovers above the obstacle at $D/c = 1$.

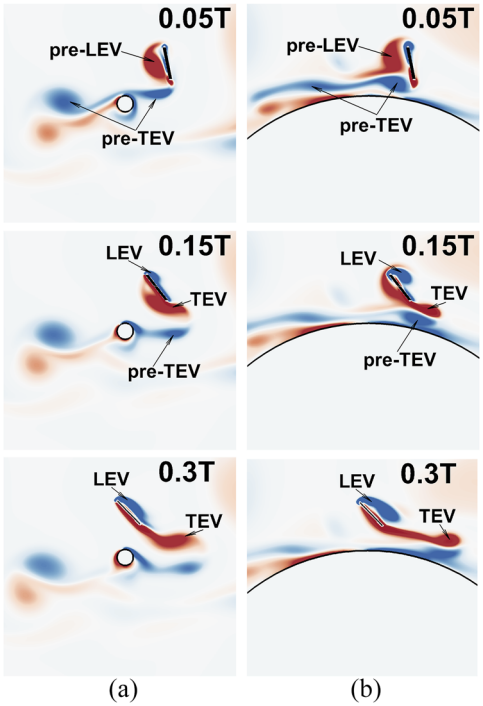

FIG. 5. Instantaneous vorticity contour for r = (a) 0.5 and (b) 12 at $D/c = 1$. The contour level ranges from $-25U/c$ to $+25U/c$.

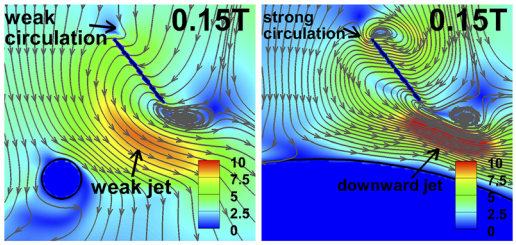

FIG. 6. Velocity magnitude contour and streamlines for r = (a) 0.5 and (b) 12 at D/c = 1.

closer to the wing and results in stronger vortex-wing interaction. Just after reversal at t/T = 0.05 for r = 12, the previous downstroke LEV and TEV are strongly obstructed because of the limited gap between TE and obstacle surface, as shown in Fig. 5(b). So the wake-capture effect between the wing and pre-LEV is intensified and lift generation enhanced. However, as the obstacle size shrinks from 12 to 0.5, the gap becomes wider and obstruction weaker, which forms a downward passage to encourage the pre-LEV to slide down along the wind side, pinch off the shedding pre-TEV, diminish the pre-LEV and pre-TEV strength, and then weaken the new LEV strength and the wake-capture effect. In Fig. 4(a), the first C_L peak of r = 0.5 is much lowered, smaller than **NO**. In Fig. 5, when the wing advances upstroke to t/T = 0.15, one can notify that the pre-LEV of r = 0.5 convects almost along the wind side through the gap and fails to pass over the LE to strengthen the new LEV so that the wake-capture effect has been greatly undermined and aerodynamic force diminishes. For r = 12, the pre-LEV partially crosses over the LE, merges with the new LEV which boosts the vortex strength, and partially moves along the wind side to form a strong vortex pair with the pre-TEV, which both contributes to higher lift and drag generation. The new LEV and shedding TEV pair are strong for r = 12 around t/T = 0.3 (second force peak). However, the LEV tends to detach from the LE compared with smaller obstacle situation. Such reduces the force generation and makes the second peak comparable with r = 4. Figure 6 displays the velocity contour and streamline for r = 0.5 and 12 at t/T = 0.15. The maximum velocity magnitude is higher under the wing for r = 12, and a strong circulation around LE and a downward jet are formed, which both contribute to the force generation. As for r = 0.5, nearly no circulation appears at the LE. The flow transfers more vertically through the wide gap, causing

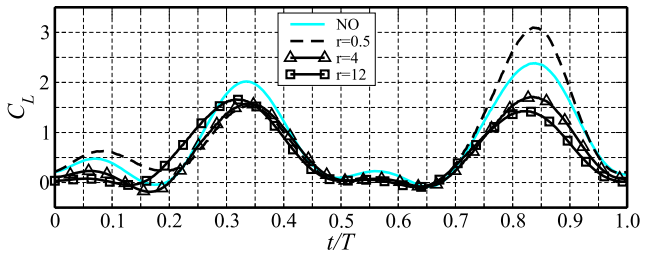

FIG. 7. Histories of the lift coefficient for r = 0.5, 4, 12, and nonobstacle in one cycle when the wing hovers above the obstacle at D/c = 3.

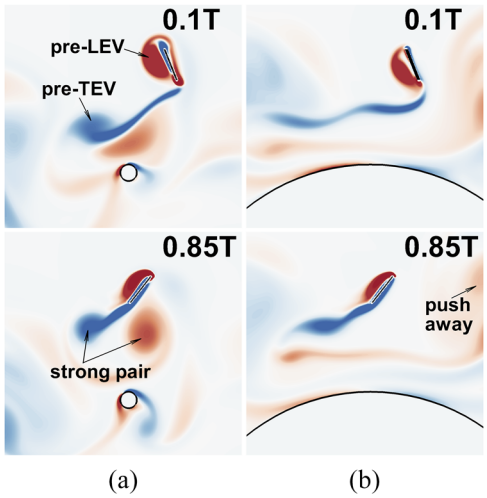

FIG. 8. Instantaneous vorticity contour for r = (a) 0.5 and (b) 12 at D/c = 3. The contour level ranges from $-25U/c$ to $+25U/c$.

low-velocity gradient and much weaker jet. Such passage effect between the wing and small obstacle causes reversed force change, which lacks discussion in the previous literature.

2. Medium and recovery distance region

Figure 7 displays the time-dependent lift coefficient over one period in the medium distance region of D/c = 3 for r = 0.5, 4, and 12. At this distance, also four high peaks appear during one cycle. The second peaks of each curve are very close, and the third peaks almost vanish. At t/T = 0.1 in Fig. 7, the first peak is higher for r = 0.5 than the other three. Figure 8(a) shows that at t/T = 0.1, the inadequate blockage allows the pre-LEV and pre-TEV to be less stretched and develop more vertically when wing hovers above the obstacle of r = 0.5. Compared with r = 12 in Fig. 8(b), the positive pre-LEV is greater, and interacting with LE, the pre-TEV remains conserved and pairs with last cycle positive TEV, which helps enhance the force generation. For r = 12, the strong obstruction forms a horizontal shear effect to force the flow to two sides of the obstacle so that the pre-LEV convects more along the wind side and is squeezed to detach from the wing, instead of crossing over the LE and interacting with the wing. The current shedding negative TEV is extensively

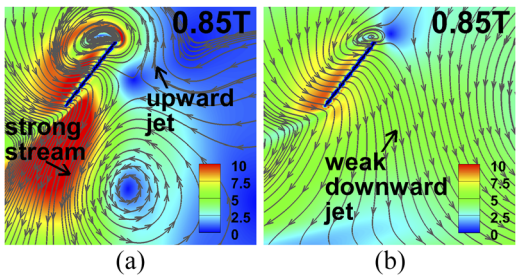

FIG. 9. Velocity magnitude contour and streamlines for r = (a) 0.5 and (b) 12 at D/c = 3.

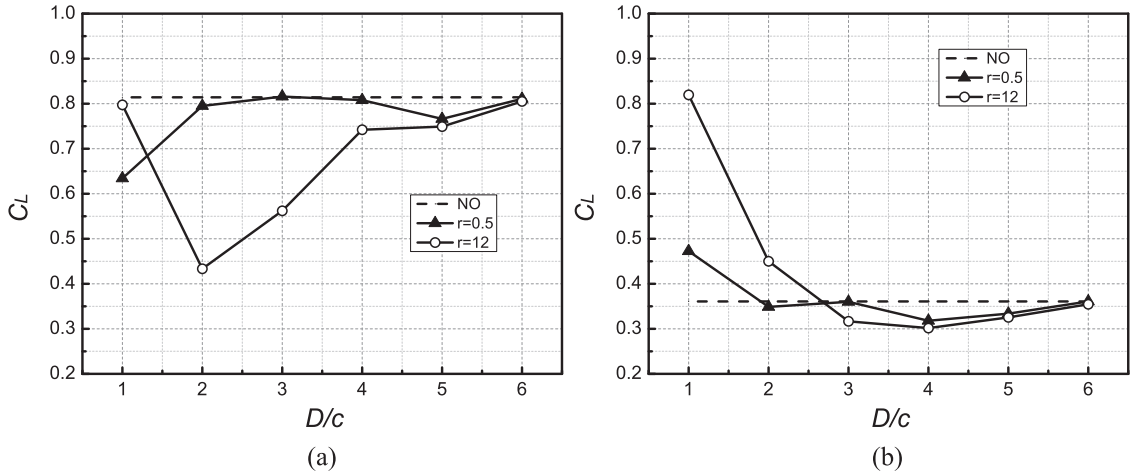

FIG. 10. Time-averaged lift coefficients when the wing hovers above the obstacle with β = (a) $\pi/8$ and (b) $\pi/3$.

elongated, and positive pre-TEV has been separated into two parts and pushed away from the wing. The fourth peaks at $t/T = 0.85$ show the largest difference among four curves. The peak value diminishes as r increases from 0.5 to 12. From vorticity contour, the strongest and closest vortex pair appears for $r = 0.5$. The existing small obstacle makes the space large enough to keep previous positive TEV least stretched and move toward the wing during the upstroke. Meanwhile, the current negative TEV also remains unstretched and pairs with the pre-TEV. The generation of such strong vortex pair gives rise to high lift at $t/T = 0.85$ as shown in Fig. 7. For $r = 12$, the previous positive TEV is pushed away from the wing in the horizontal direction and dissipates fast because of the stretching. The current negative TEV is also squeezed into two parts and separated with the last TEV, which abates the strength of TEV pair as well as force generation. From such circumstance, the TEV pair plays a significant role during the upstroke. Figure 9 shows that the velocity magnitude under the wing of $r = 0.5$ is much stronger than that of $r = 12$. Strong upward jet and downward stream around the wing in Fig. 9(a) bring higher lift generation compared with weak downward jet and no upward jet for $r = 12$. When D/c increases to 4, space is adequate for all obstacle to form strong wing vortex interaction so that all forces increase from $D/c = 3$ to 4 in Figs. 3(a) and 3(b).

Finally, as the D/c continues increasing above 5, force recovery occurs for all situations as the obstacle becomes far away and affects the aerodynamics little.

3. Effect of flapping angle

Figure 10 shows the time-averaged lift coefficients over 15 cycles with respect to D/c for two flapping angle amplitudes: $\beta = \pi/8$ and $\pi/3$. For $\beta = \pi/8$, all the lift coefficients are less than the **NO** value. The curve of $r = 12$ shows a V-shape trend while $r = 0.5$ a reverse V-shape. When flapping close to the obstacle ($D/c = 1$), C_L of $r = 12$ is at the highest point, slightly below **NO**, then decreases to the low peak at $D/c = 2$, and gradually recovers to the **NO** value. C_L of $r = 0.5$ shows a reversed change: force reduction in close distance of $D/c = 1$, enhancement in a medium distance of $D/c = 3$, and finally recovery. Such force change discrepancy between small and large obstacles is consistent with that of $\beta = \pi/4$. However, as the β increases to $\pi/3$, curves of $r = 0.5$ and 12 in Fig. 10(b) show the same trend analogous to each other: force becomes enhanced at $D/c = 1$, then decreases to the minimum, and finally approaches the **NO** value. The minimum lift occurs at the same distance of $D/c = 4$ for both $r = 0.5$ and 12.

The force histories and flow fields are given in Figs. 11–14. For $\beta = \pi/8$ in Fig. 11, two black curves ($r = 0.5$ and 12 at $D/c = 1$) are quite periodic during downstroke and upstroke. Only one high peak occurs during each half stroke for both curves: at $t/T = 0.26(0.76)$ for $r = 0.5$ and $t/T = 0.16(0.66)$ for $r = 12$. When $\beta = \pi/8$, the wing pitches up less so that the gap becomes narrower. Figures 12(a) and 12(b) display the vorticity contours, and it can be seen at the first lift peak ($t/T = 0.16$) for $r = 12$, the entire pre-LEV crosses over the LE and merge to generate a stronger new LEV. Also, a strong vortex pair consisting of the TEV and pre-TEV is formed, also helping generate higher lift. For $r = 0.5$, the LEV is weaker and the TEV pair is pushed away from such that the first peak is lower. As D/c increases to 2, the red curve of $r = 0.5$ in Fig. 11 shows higher lift peaks than the curve of $r = 12$. At $t/T = 0.78$ in Fig. 12(d), the enlarged gap under TE makes the LEV and TEV convect along the wing and slip through the gap, which leads to weakened wake-capture effect and dissipated TEV pair compared with that of $r = 0.5$ in Fig. 12(c).

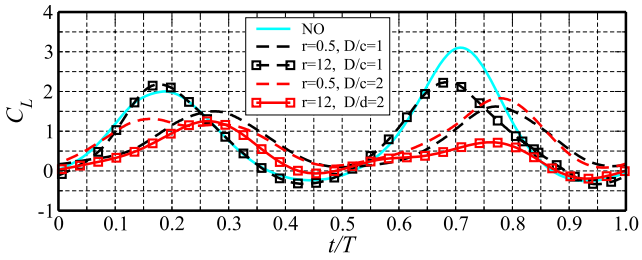

FIG. 11. Histories of the lift coefficient for $\beta = \pi/8$, $r = 0.5$, 12, and nonobstacle in one cycle when the wing hovers above the obstacle.

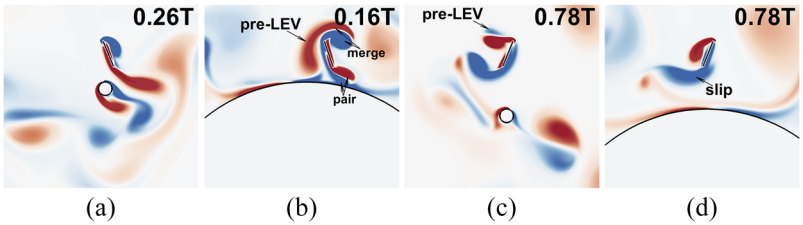

FIG. 12. Instantaneous vorticity contour when flapping above an obstacle with $\beta = \pi/8$ for (a) $r = 0.5$, $D/c = 1$; (b) $r = 12$, $D/c = 1$; (c) $r = 0.5$, $D/c = 2$; and (d) $r = 12$, $D/c = 2$. The contour level ranges from $-25U/c$ to $+25U/c$.

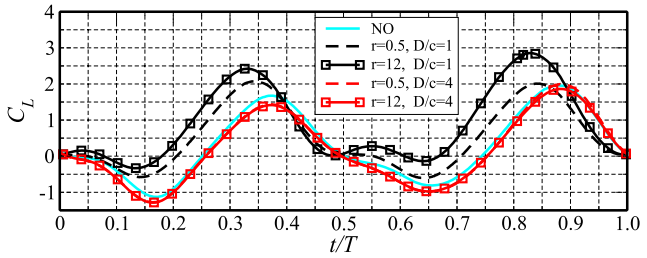

FIG. 13. Histories of the lift coefficient for $\beta = \pi/3$, $r = 0.5$, 12, and nonobstacle in one cycle when the wing hovers above the obstacle.

For $\beta = \pi/3$ in Fig. 13, black curves for the force enhancement region at $D/c = 1$ are generally higher than red curves for the force reduction region at $D/c = 4$. Each curve experiences a low negative peak around $t/T = 0.15(0.65)$ and a high peak around $t/T = 0.35(0.85)$ during each half stroke. At $t/T = 0.15$ in Fig. 14, all LEVs are not effectively formed and barely seen only at $r = 12$, $D/c = 1$ due to small flapping angle, so the lee side suction effect fails. All wake-capture effect is weakened due to the wider gap as well. The pre-LEV tends to detach from the wind side, especially for $r = 12$ at $D/c = 4$ and pair with the pre-TEV, which results in negative lift force. At $t/T = 0.35$, LEVs are similar for all situations. The narrower gap of $D/c = 1$ forms a stronger TEV pair, which leads to a higher lift. So when flapping angle amplitude is large, the finite obstacle effect becomes more uniform/comparable.

B. Effect of top obstacle

Figure 15 shows lift coefficients averaged over 15 cycles when the wing hovers under an obstacle. The most evident observation is that almost all lift forces are increased compared with nonobstacle hovering no matter what the obstacle size and distance are. For all cases, the forces reach the maximum at $D/c = 1$ and larger obstacle leads to greater force enhancement. The highest $C_L = 1.29$ shows up at $D/c = 1$ for $r = 12$, higher than the wing hovers above an obstacle at the same D/c. Then, the forces decrease monotonically as the clearance D/c enlarges. Finally, they approach the nonobstacle value when $D/c \geq 6$. The forces descend fast from $D/c = 1$ to 2. The effect becomes relatively weak as $D/c \geq 2$, and after that forces do not change much. For $r \leq 1$, the lift force change is not obvious, only 10.2% when D/c varies from 1 to 6. Force change tendency shows that only large and close obstacle influences the aerodynamic performance of the wing effectively when hovering under it.

The time-dependent force change in one cycle for $D/c = 1$ is shown in Fig. 16 associated with vorticity contour in Fig. 17. The curves of **NO** and $r = 0.5$ are quite similar to each other, meaning small obstacle above the wing affects aerodynamics very little. We can notify that the shedding vortices of $r = 12$ transfer more upward along with the obstacle than downward and stay around the wing, which is not observed for cases of the smaller obstacle. At $t/T = 0.15$, the location of pre-TEV from the last stroke is vertically higher than the other two. From $t/T = 0.15$ to 0.77, this pre-TEV keeps staying on the left side of the wing with low mobility other than transferring downward, which results in very complicated vortex merging and interacting. Also, a new LEV of $r = 12$ is strongly formed; the pre-LEV is partially squeezed to pass through the clearance and

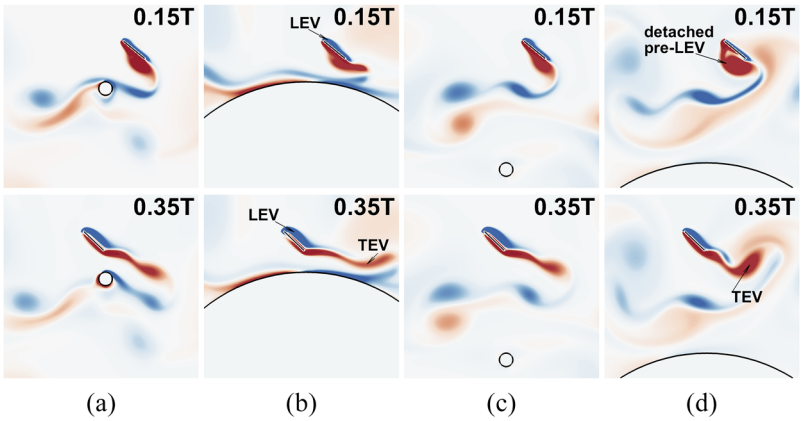

FIG. 14. Instantaneous vorticity contour when flapping above an obstacle with $\beta = \pi/3$ for (a) $r = 0.5$, $D/c = 1$; (b) $r = 12$, $D/c = 1$; (c) $r = 0.5$, $D/c = 4$; and (d) $r = 12$, $D/c = 4$. The contour level ranges from $-25U/c$ to $+25U/c$.

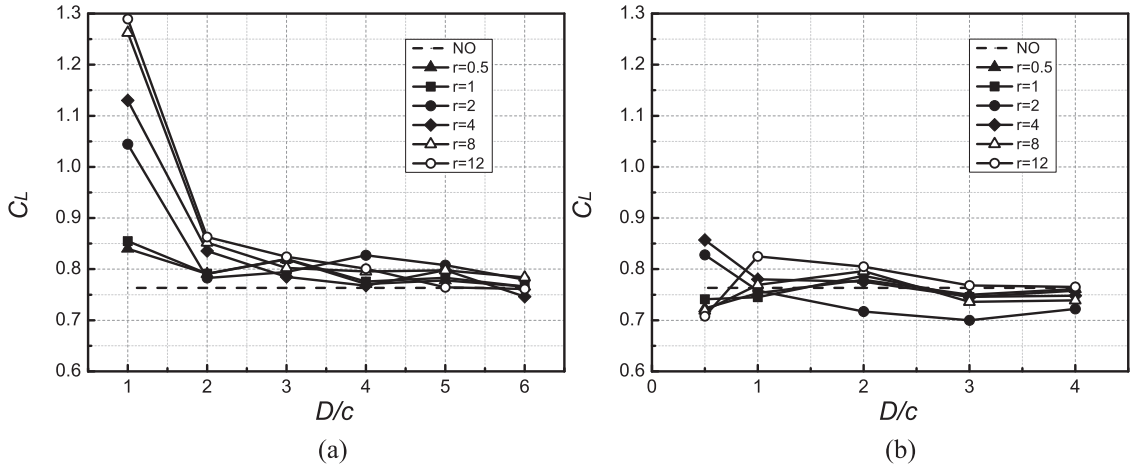

FIG. 15. Time-averaged lift coefficients when the wing hovers (a) under and (b) on the right of the obstacle.

merge with the new LEV and partially interacts with the wing. Both enhance the lift generation by increasing the wake-capture effect during the downstroke. Figure 18 illustrates the velocity field and streamlines for $r = 4$ and 12 at $t/T = 0.15$. It can be seen that a strong circulation occurs around the LE of $r = 12$ with high-velocity magnitude, which forms a strong LEV and high lift force. However, for the case of $r = 4$, the streamlines are almost perpendicular to the LE and pass through the relatively wide gap such that the LEV is barely generated and low lift force is created.

At $t/T = 0.35$, the LEV is pinched off and detaches from the LE for $r = 12$, which lowers the second lift peak. For $r = 4$, the LEV attaches to the lee side of the wing and a strong TEV pair has been formed under the wing, assisting aerodynamic force enhancement. From $t/T = 0.65$ to 0.77 in Fig. 16, all curves are ascending. During this period, the LEV is being generated and a TEV pair has been formed, which are beneficial to the force generation. Figure 17 shows that at $t/T = 0.77$, the LEV development is faster and stronger for $r = 12$ than that of $r = 4$. Also, the current TEV closely pairs up with the TEV from downstroke and merges with the TEV from the last cycle, which doubles the lift enhancement effect so that the peak of $r = 12$ appears earlier and higher. Gradually as time advances, the LEV grows and the TEV pairs move toward the wing, both curves of $r = 0.5$ and 4 reach the peak round at $t/T = 0.85$ with a lower value compared with the peak of $r = 12$.

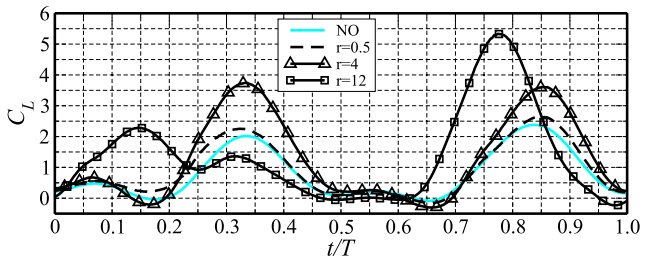

FIG. 16. Histories of the lift coefficient for $r = 0.5$, 4, 12, and non-obstacle in one cycle when the wing hovers under the obstacle at $D/c = 1$.

C. Effect of side obstacle

The horizontal effect is studied when the wing hovers on the left/right of the obstacle. Considering the symmetry, only wing flapping on the right is simulated with results shown in Fig. 15. It shows that the horizontal obstacle effect is comparably weak compared to

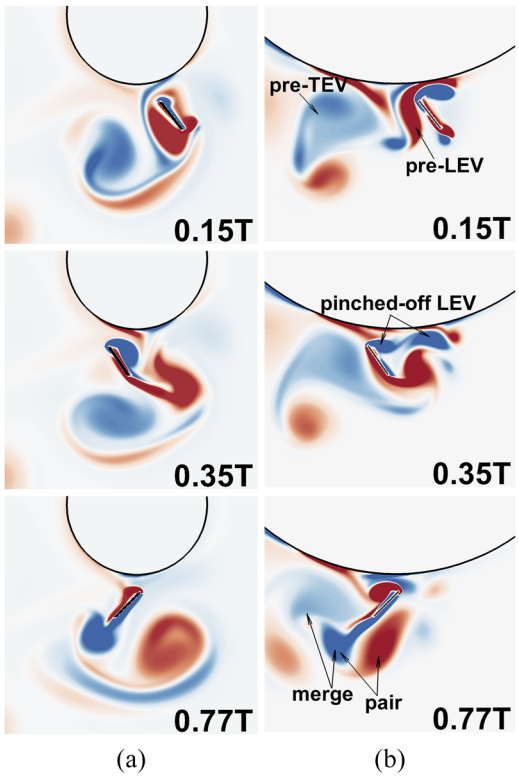

FIG. 17. Instantaneous vorticity contour for r = (a) 4 and (b) 12 at $D/c = 1$ when obstacle on top. The contour level ranges from $-25U/c$ to $+25U/c$.

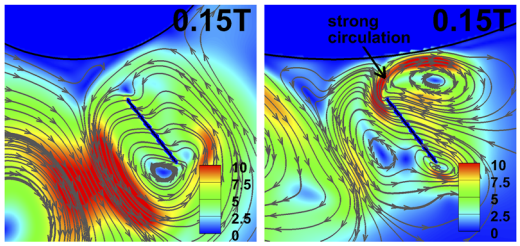

FIG. 18. Velocity magnitude contour and streamlines for r = (a) 4 and (b) 12 at D/c = 1 with obstacle on top.

the vertical effect, yet consistent. At D/c = 0.5, the lift forces for r = 0.5, 1, 8, and 12 are reduced, and the values are slightly below the nonobstacle dashed-line. Then as the distance enlarges, forces increase to a small peak, the highest of which occurs at D/c = 1 for r = 12, obtaining 8.1% force improvement. Finally, all the curves fall back to the nonobstacle value. For r = 2 and 4, the forces are enhanced at D/c = 0.5, however only 8.4% and 12.3% improvement, respectively. Then, the force change shows reduction and recovery stages, however, values relatively small.

Figures 19 and 20 display the force history and vorticity field for r = 0.5, 4, and 12 at D/c = 0.5. The force history shows four high peaks for each curve. The first, second, and fourth peaks of NO are all above those of r = 0.5 and 12. At t/T = 0.07 and 0.81 when the stroke reversal and fast translational rotation happen, the peaks of r = 4 are the highest among all curves. Since the obstacle stays on the side, the LEV is affected least compared with the obstacle in vertical locations. In Fig. 20, all LEVs keep attached to the LE with similar strength and motion. On the other hand, shedding TEVs are the main influence on force change. At t/T = 0.07, previous shedding TEVs pair up close to the wing for r = 4 and contributes to the lift increase. As for r = 12, positive pre-TEV is pushed away and lowers the lift. At t/T = 0.81 when moving away from the obstacle, the pre-TEV from downstroke is pushed away due to the obstruction, not able to pair with the current negative shedding TEV and interact with the wing for r = 12, similar as in Fig. 8(c) at t/T = 0.85. As for the case of r = 4, stronger and closer TEV pair obviously increases the lift to be greater than others.

Since the wing hovers on the right of the obstacle, the side force is investigated as well by averaging the horizontal force F_H over 15

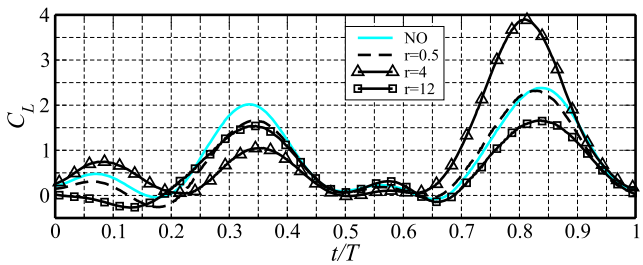

FIG. 19. Histories of the lift coefficient for r = 0.5, 4, 12, and nonobstacle in one cycle when the wing hovers on the right the obstacle at D/c = 0.5.

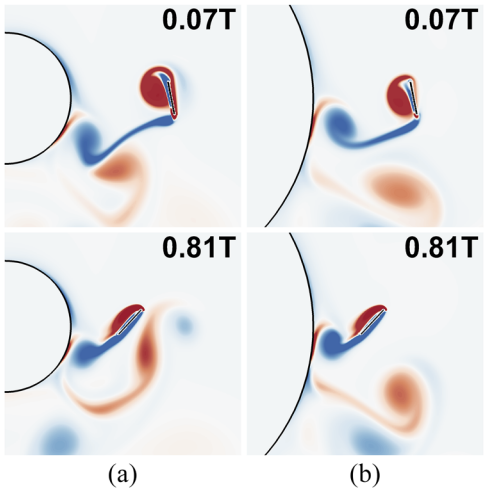

FIG. 20. Instantaneous vorticity contour for r = (a) 4 and (b) 12 at D/c = 0.5 when obstacle on the left. The contour level ranges from $-25U/c$ to $+25U/c$.

cycles and nondimensionalized as follows:

$$C_H = \frac{F_H}{(0.5\rho_f U^2 c)}. \tag{9}$$

Figure 21 displays C_H for nonobstacle hovering and cases of r = 0.5, 4, and 12. Positive C_H means force pushing the wing away from the obstacle, negative attracting the wing toward the obstacle. Comparing C_H with C_L and C_D, the magnitude is much smaller because the horizontal force counterbalances between downstroke and upstroke. The dashed line of **NO** is plotted as a reference. For the case of r = 4 and 12, side forces are all negative and non-negligible at $D/c \leq 3$, which means that the wing is attracted to the obstacle and may cause potential risk.

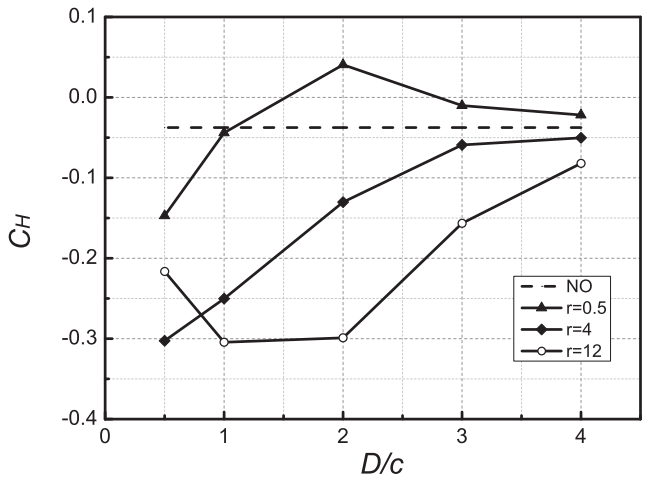

FIG. 21. Time-averaged horizontal force coefficients when the wing hovers on the right of the obstacle.

VI. CONCLUSIONS

The finite obstacle effect on the aerodynamic performance of a hovering wing has been investigated using the immersed boundary method. The wing of chord length c normal hovers above, under, and on the side of a finite circular obstacle with diameter ranging from $0.5c$ to $12c$. Results reveal that when the obstacle size equals or exceeds $2c$, the finite obstacle effect shows similarity to the ground effect with force enhancement, reduction, and recovery. As the obstacle size shrinks less than $2c$, lift and drag change shows the opposite trend: decrease as hovering in close distance ($D/c < 3$), increase in medium distance ($3 \le D/c < 5$), and then recover to free normal hover. When flapping angle amplitude increases to $\pi/3$, all the force change tends to be consistent with ground effect. When hovering close to a smaller obstacle, the gap passage between the TE and obstacle surface impedes the LEV forming, wake-capture, and TEV pairing, which undermine the force generating and aerodynamic efficiency. When hovering in the medium distance to the smaller obstacle, favorable weak obstruction keeps the TEVs more conserved, thereby strengthening the pairing and enhancing the force.

The top finite boundary effect is consistent for different-sized obstacles: the force increases monotonically as the distance decreases. A large obstacle induces more increase. However, such force enhancement decays fast as long as $D/c \ge 2$; all the lift increase is less than 10% no matter what size of the obstacle is. The side effect is weaker compared with the down or top obstacle. All force changes under such circumstance are less than 13% compared to the nonobstacle results.

Such study provides more knowledge in understanding the mechanisms of the finite obstacle effect when the insect flies close to it. Since the real working condition of future bio-inspired MAV is challenging, it is necessary to consider more complicated boundaries and study how the active control would adjust the flight accommodating to the real-time situation.

ACKNOWLEDGMENTS

This research is supported by the National Natural Science Foundation of China (Grant No. 11702297) and the National Key Research and Development Program of China (Grant No. 2017YFB0202802).

REFERENCES

[1]C. P. Ellington, "The novel aerodynamics of insect flight: Applications to micro-air vehicles," J. Exp. Biol. **202**, 3439–3448 (1999).
[2]N. Bradshaw and D. Lentink, "Aerodynamic and structural dynamic identification of a flapping wing micro air vehicle," in *26th AIAA Applied Aerodynamics Conference* (AIAA, 2008).
[3]S. P. Sane, "The aerodynamics of insect flight," J. Exp. Biol. **206**, 4191–4208 (2003).
[4]Z. J. Wang, "Dissecting insect flight," Annu. Rev. Fluid Mech. **37**, 183–210 (2005).
[5]Y. Lian, W. Shyy, D. Viieru, and B. Zhang, "Membrane wing aerodynamics for micro air vehicles," Prog. Aerosp. Sci. **39**, 425–465 (2003).
[6]R. J. Bomphrey, T. Nakata, N. Phillips, and S. M. Walker, "Smart wing rotation and trailing-edge vortices enable high frequency mosquito flight," Nature **544**, 92–95 (2017).
[7]T. Y. Wu, "Fish swimming and bird/insect flight," Annu. Rev. Fluid Mech. **43**, 25–58 (2011).
[8]P. J. Wilkin and M. H. Williams, "Comparison of the aerodynamic forces on a flying sphingid moth with those predicted by quasi-steady theory," Physiol. Biochem. Zool. **66**, 1015–1044 (1993).
[9]C. P. Ellington, C. van den Berg, A. P. Willmott, and A. L. R. Thomas, "Leading-edge vortices in insect flight," Nature **384**, 626–630 (1996).
[10]M. H. Dickinson, F. Lehmann, and S. P. Sane, "Wing rotation and the aerodynamic basis of insect flight," Science **284**, 1954–1960 (1999).
[11]J. M. Birch and M. H. Dickinson, "The influence of wing-wake interactions on the production of aerodynamic forces in flapping flight," J. Exp. Biol. **206**, 2257–2272 (2003).
[12]J. Han, Y. Zhang, and G. Chen, "Effects of individual horizontal distance on the three-dimensional bionic flapping multi-wings in different schooling configurations," Phys. Fluids **31**, 041903 (2019).
[13]J.-S. Han, H.-Y. Kim, and J.-H. Han, "Interactions of the wakes of two flapping wings in hover," Phys. Fluids **31**, 021901 (2019).
[14]B. Singh and I. Chopra, "Insect-based hover-capable flapping wings for micro air vehicles: Experiments and analysis," AIAA J. **46**, 2115–2135 (2008).
[15]W. Shyy, H. Aono, S. K. Chimakurthi, P. Trizila, C. Kang, C. E. S. Cesnik, and H. Liu, "Recent progress in flapping wing aerodynamics and aeroelasticity," Prog. Aerosp. Sci. **46**, 284–327 (2010).
[16]D. Kim and M. Gharib, "Experimental study of three-dimensional vortex structures in translating and rotating plates," Exp. Fluids **49**, 329–339 (2010).
[17]C. A. Ozen and D. Rockwell, "Three-dimensional vortex structure on a rotating wing," J. Fluid Mech. **707**, 541–550 (2012).
[18]W. Shyy, P. Trizila, C. Kang, and H. Aono, "Can tip vortices enhance lift of a flapping wing," AIAA J. **47**, 289–293 (2009).
[19]U. Pesavento and Z. J. Wang, "Flapping wing flight can save aerodynamic power compared to steady flight," Phys. Rev. Lett. **103**, 118102 (2009).
[20]H. Deng, Y. Xu, D. Chen, H. Dai, J. Wu, and F. Tian, "On numerical modeling of animal swimming and flight," Comput. Mech. **52**, 1221–1242 (2013).
[21]T. Gao and X. Lu, "Insect normal hovering flight in ground effect," Phys. Fluids **20**, 087101 (2008).
[22]J. Zerihan and X. Zhang, "Aerodynamics of gurney flaps on a wing in ground effect," AIAA J. **39**, 772–780 (2001).
[23]H. Lu, K. B. Lua, T. T. Lim, and K. S. Yeo, "Ground effect on the aerodynamics of a two-dimensional oscillating airfoil," Exp. Fluids **55**, 1787 (2014).
[24]M. Maeda and H. Liu, "Ground effect in fruit fly hovering: A three-dimensional computational study," J. Biomech. Sci. Eng. **8**, 344–355 (2013).
[25]T. Van Truong, D. Byun, M. J. Kim, K. J. Yoon, and H. C. Park, "Aerodynamic forces and flow structures of the leading edge vortex on a flapping wing considering ground effect," Bioinspiration Biomimetics **8**, 036007 (2013).
[26]H. Lu, K. B. Lua, Y. J. Lee, T. T. Lim, and K. S. Yeo, "Ground effect on the aerodynamics of three-dimensional hovering wings," Bioinspiration Biomimetics **11**, 066003 (2016).
[27]J. Su, J. Tang, C. Wang, and J. Yang, "A numerical investigation on the ground effect of a flapping-flying bird," Phys. Fluids **25**, 093101 (2013).
[28]D. Kolomenskiy, M. Maeda, T. Engels, H. Liu, K. Schneider, and J. Nave, "Aerodynamic ground effect in fruitfly sized insect takeoff," PLoS One **11**, e0152072 (2016).
[29]L. Wang and R. W. Yeung, "Investigation of full and partial ground effects on a flapping foil hovering above a finite-sized platform," Phys. Fluids **28**, 071902 (2016).
[30]X. Meng, "Ceiling effects on the aerodynamics of a flapping wing at hovering condition," Phys. Fluids **31**, 051905 (2019).
[31]J. D. Eldredge, "Numerical simulation of the fluid dynamics of 2d rigid body motion with the vortex particle method," J. Comput. Phys. **221**, 626–648 (2007).
[32]R. Mittal, H. Dong, M. Bozkurttas, F. M. Najjar, A. Vargas, and A. Von Loebbecke, "A versatile sharp interface immersed boundary method for incompressible flows with complex boundaries," J. Comput. Phys. **227**, 4825–4852 (2008).
[33]H. Luo, R. Mittal, X. Zheng, S. Bielamowicz, R. J. Walsh, and J. K. Hahn, "An immersed-boundary method for flow-structure interaction in biological systems with application to phonation," J. Comput. Phys. **227**, 9303–9332 (2008).

[34]Z. J. Wang, J. M. Birch, and M. H. Dickinson, "Unsteady forces and flows in low Reynolds number hovering flight: Two-dimensional computations vs robotic wing experiments," J. Exp. Biol. **207**, 449–460 (2004).
[35]H. Luo, B. Yin, H. Dai, and J. Doyle, "A 3D computational study of the flow-structure interaction in flapping flight," in *AIAA Aerospace Sciences Meeting Including the New Horizons Forum and Aerospace Exposition* (AIAA, 2010).
[36]B. Yin and H. Luo, "Effect of wing inertia on hovering performance of flexible flapping wings," Phys. Fluids **22**, 111902 (2010).
[37]H. Luo, H. Dai, P. F. De Sousa, and B. Yin, "On the numerical oscillation of the direct-forcing immersed-boundary method for moving boundaries," Comput. Fluids **56**, 61–76 (2012).
[38]F. Tian, H. Luo, J. Song, and X. Lu, "Force production and asymmetric deformation of a flexible flapping wing in forward flight," J. Fluid Struct. **36**, 149–161 (2013).
[39]F. Tian, J. Young, and J. C. S. Lai, "Improving power-extraction efficiency of a flapping plate: From passive deformation to active control," J. Fluid Struct. **51**, 384–392 (2014).